This article has been accepted for publication in IEEE Robotics and Automation Letters. This is the author's version which has not been fully edited and content may change prior to final publication. Citation information: DOI 10.1109/LRA.2025.3559829

Hybrid tension and configuration control of cable-driven hyper-redundant robots for high accuracy and stability

Zhenpu Zhu, Ziqing Li, Zhanxuan Peng, Chao Liu, *Member, IEEE* and Guoying Gu, *Senior Member, IEEE*

***Abstract*—Due to the advantages of dexterity and adaptability, cable-driven hyper-redundant robots (CDHRRs) are promising for detection in confined spaces like narrow internal cavities. However, due to redundant degrees of freedom (DoFs), CDHRRs are susceptible to the singular configuration, which aggravates the difficulty of high-accuracy control and high-stable motion. To solve these problems, this work proposes hybrid tension and configuration control to improve motion accuracy and stability. Firstly, a CDHRR model with structural optimization and friction reduction is developed. The quasi-static and cable-hole length estimation models are obtained, including cable-hole friction, cable-hole interval, and cable deformation. Subsequently, single and multi-segment controllers are designed. The controller can distribute tension in the expected range with the above design while featuring high accuracy, responsiveness, and stability. The control algorithm optimizes configuration with an average error under 1.00°. Moreover, the controller reaches the target with controllable forces in 1.0 s and flattens the fluctuations within 0.3 s. The controller can be implemented into automatic zeroing and tip loading. Experimental results demonstrate that the proposed controller features speedy automatic zeroing (in 4 mins) and low angle tracking errors (less than 1.50°) under various tip loads.**

***Index Terms*—Soft Robot Applications, Hyper-redundant robot, Friction reduction, Hybrid control, Stepwise force**

I. Introduction

CDHRRS have gained continuously growing attention because of their high flexibility and slim body size [1–3]. Thus, they are widely applied in various fields, such as minimally invasive surgery [4], aerospace [5], and nuclear industries [6]. Specialized missions call for corresponding control methods.

In early research, open-loop controllers were widely utilized to steer CDHRRs to desired positions [7]. Based on applied models, open-loop controllers are categorized into kinematics-based open-loop controllers [8, 9] and dynamics-based open-loop controllers [10]. The kinematic controllers use geometric models and spatial coordinate transformation matrices to establish mapping relationships among cables, joints, and end-effectors [8]. They achieve good tracking performance, load carrying, and grasping capacity in complex scenarios like underwater environments [9]. The dynamics controllers integrate forward and inverse kinematics with recursive Newton-Euler dynamics to compute. They control motion and compensate for cable tension and contact forces effectively [10]. To improve control accuracy, friction-feedforward compensation is considered. The friction in the drive system is investigated, and a dynamic model is established by Kane's method [11]. Furthermore, neural networks are also applied to avoid the complexity of modeling nonlinear dynamics [12, 13]. Though straightforward, open-loop controllers are prone to position errors, leading to low control accuracy.

Therefore, closed-loop controllers are needed for higher control precision. The primary challenges involve the arrangement of antagonistic cables and tension control [14]. Several approaches had been proposed, such as fuzzy controllers [15], [16], antagonistic impedance controllers [17, 18], and puller-follower controllers [19, 20]. However, for robots equipped solely with force sensors [20], accurately measuring and compensating for cable elongation errors presents significant challenges. Struggling with tension estimation, the precision performance fell short of expectations.

Consequently, the demand for CDHRRs incorporating both force and position sensors is prompted [20]. With the improved structure of the integrated sensor, the hybrid control method is proposed [21]. By simultaneously tracking position and force, the stability of the system is enhanced [22]. However, some controllers are assessed in small-scale environments [23], or validated in simulation [24]. Lacking of physical verification platform, these controller's efficiency diminished at large scales, potentially resulting in instability.

To tackle these difficulties, we propose a hybrid tension and configuration control method for CDHRRs to improve accuracy and stability. Firstly, a CDHRR model with structural optimization and friction reduction is designed. To enhance control accuracy, geometric models and cable properties are considered. The kinematic and quasi-static models are analyzed, and the cable-hole length estimation algorithm is developed. Based on the model, single and multi-segment hybrid tension and configuration controllers with stepwise force arrangement are established. Experimental results demonstrate optimization and control efficiency. Controllers are further validated in automatic zeroing and tip loading.

The main contributions of this work are summarized as follows.

(1) This study presents a theoretical model that integrates structural optimization and friction-reduction techniques. Specifically, the incorporation of a double side chamfered cable guide disk with a low friction coefficient represents

Manuscript received: December 17, 2024; Revised: February 18, 2025; Accepted: March 23, 2025. This paper was recommended for publication by Editor Cecilia Laschi upon evaluation of the Associate Editor and Reviewers' comments. This work was supported in part by the National Natural Science Foundation of China (Grant No. 52025057 and T2293725), the Science and Technology Commission of Shanghai Municipality (Grant No. 24511103400) and Xplorer Prize. *(Corresponding Author: Guoying Gu)*

The authors are with the State Key Laboratory of Mechanical System and Vibration, Robotics Institute, School of Mechanical Engineering, Shanghai Jiao Tong University, Shanghai 200240, China (e-mail: zhuzhenpu@sjtu.edu.cn; 627851623@qq.com; steven2606@sjtu.edu.cn; aalon@sjtu.edu.cn; guguoying@sjtu.edu.cn).

Digital Object Identifier (DOI): see top of this page.

a distinct advancement over prior designs, enhancing engineering applicability. Validation on SJTU-Snake III platform confirms the model's accuracy and efficiency, addressing limitations in previous approaches.

(2) A hybrid tension and configuration control method is developed by integrating the optimization strategy with detailed geometric models and cable-specific properties. By incorporating cable length estimation algorithm, the cable-hole discrepancy is eliminated, and the real-time tension estimation algorithm enables precise configuration control. Experiments on SJTU-Snake III, including automatic zeroing and tip-loading tests, demonstrate the method's efficiency and its advantages over existing techniques.

The rest of this article is organized as follows. Section II introduces the structural characteristics and improvements of SJTU-Snake III. The kinetics and statics models are elaborated in section III, including the mapping task and cable-hole error factors. Based on this model, the hybrid tension and configuration control methods are developed in Section IV. Section V verifies the accuracy and effectiveness of the proposed methods. Section VI concludes the article and discusses future work.

II. System Description and Optimization

The structural design of SJTU-Snake III, a CDHRR, is shown in Fig. 1(a). SJTU-Snake III comprises a motioning platform, a linear-feeding platform, a drive box, a cable-guiding mechanism, and a robotic manipulator. The linear-feeding platform is situated atop the bottom motioning platform, with the drive box mounted above it. The cable-guiding mechanism, linking the drive box to the robotic manipulator, comprises twelve 2-DoF parallel platforms. Each platform is connected in series through gimbal joints and is controlled by three driving cables.

In SJTU-Snake III, friction primarily originates from the cable traversing through the guide disks, namely cable-hole friction. The experiments for mitigation are conducted, as is shown in Fig. 1(b). Synthesizing the experimental findings, aluminum serves as the material for cable guide disks, employing a 0.5mm double-sided chamfer design. The robot is optimally designed for lightweighting via finite element analysis and topology optimization in ANSYS Workbench. Rectangular segments are excised to equalize forces and minimize mass, with rounded corners to mitigate stress concentration. The mass of SJTU-Snake III's segment and cable guide disk is 1237.8 g, achieving a 26.1% reduction. An increase in the structural safety coefficient arises after weight reduction and refinement. The robot's drive burden is alleviated, enhancing the system's mechanical performance and consequently augmenting the end-load capacity. The optimization is shown in Fig. 1(c).

As an advancement of its predecessor, SJTU-Snake III features a streamlined design with external cable routing, segment weight reduction, and friction reduction. It improves the robot's aspect ratio, size of the workspace, end-loading ability, and ease of maintenance. Simultaneously, the joint angle sensor and force sensor are integrated for instantaneous feedback. The SJTU-Snake III communication system comprises AS5600 Hall magnetic sensors, and EPOS boards, and STM32-F407VET6 boards. The comparisons between SJTU-Snakes are listed in Table I.

TABLE I
MECHANICAL DESIGN INDICATORS OF SJTU-SNAKE

Description	Version I	Version II	Version III
Outer diameter	45 mm	55 mm	55 mm
Maximum angle	27.0°	48.0°	50.7°
Total arm length	1092 mm	1800 mm	2130 mm
Aspect ratio	24.27	32.73	38.73
Total mass of arm	1.25 kg	1.45 kg	0.91 kg
End load	1.0 kg	1.5 kg	1.5 kg
Cable change time	1 week	1 week	10 mins
Sensor Configuration	null	angle	angle and force

III. Modeling and Cable-hole Length Estimation

A. Cable-hole Length Estimation Model

In practical applications, to minimize the sliding friction, the radius of the hole in the cable guide disk is designed to be larger than the radius of the cable. During actual movement, the centers of the cable and the hole do not coincide and are subject to continuous changes. This discrepancy results in a mismatch between the drive cable length calculated using a simplified model and the actual drive length, thereby causing substantial movement errors. To improve motion precision, it is imperative to model and quantify these errors. Consequently, a cable length estimation algorithm is proposed, which accounts for cable-hole interval, cable-hole friction, and cable deformation.

The cable-hole interval denotes the lateral separation between the driving cable and the hole's center. It is assumed that the centroid of the actuation cable coincides with the cable-hole center for simplification. However, the cable's contact surface shifts, leading to errors between the modeled and actual cable lengths. To address the problem, a recursive approximate solution-based cable-hole interval estimation algorithm is utilized [25]. The recursive algorithm approximates cable length using a cable-hole contact model, as is detailed in Fig. 2. The algorithm presents a modeling and computational method for the driving cable length estimation, which ensures real-time control while sustaining computational precision.

B. Quasi-Static Model

The forces at the cable-holes are shown in Fig. 3(a). Given the motion process is quasi-static, a static force analysis suffices. The force equilibrium equations of each segment are listed as:

$$T_i = \begin{cases} T_{i-1} & \text{if } \beta = 0 \\ \dfrac{T_{i-1}\sin\alpha_i}{1-\mu_i\cos\alpha_i} & \text{if } \beta = 1 \end{cases} \tag{1}$$

where T_i is the tension on the i^{th} segment. β is the state of cable-hole contact. $\beta = 0$ means that the cable and hole are not in contact, while $\beta = 1$ implies contact. α_i is the angle between i^{th} and $i+1^{st}$ segment.

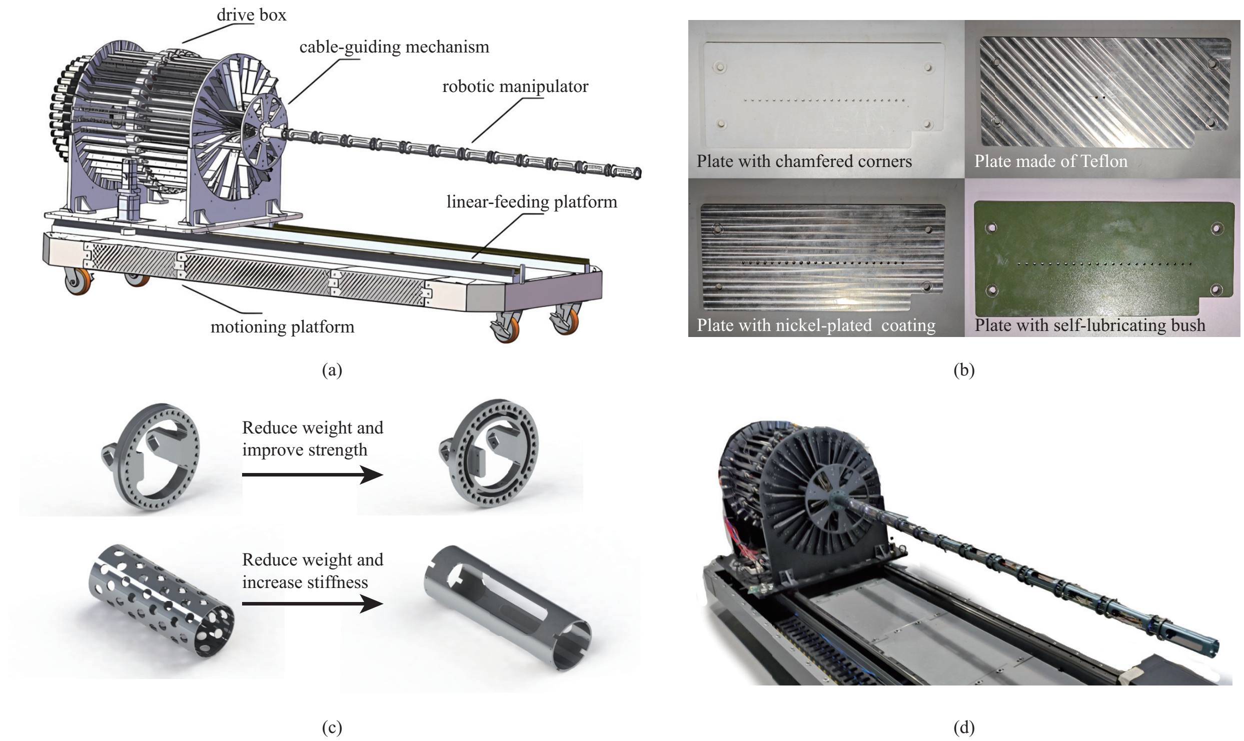

Fig. 1. (a) Structural design of SJTU-Snake III. (b) Friction measurement plates are designed for cable-hole friction experiments. (c) Lightweight segment design based on finite element analysis and topology optimization. (d) Overall assembly of SJTU-Snake III.

Both α_i and β are calculated using the cable-hole interval calculation algorithm. μ_i is the friction coefficient. Since T_i is approximated by the force sensor, only μ_i needs to be calculated. The experiments conducted in Fig. 1(b) show that the friction coefficient does not depend on velocity and contact area but varies with the tilt angle and the stretching-relaxing process. A linear regression with the cosine of the tilt angle (α) as the independent variable and the friction coefficient as the dependent variable is depicted in Fig. 3(b). The experimental data corroborates linear characteristics, and the Stribeck model, similar to the Coulomb model, is applicable.

The cable deformation refers to the elastic phase displacement. Length discrepancies are due to cumulative errors, with each segment's cable operating independently. The Newton-Euler approach is employed to deduce the equilibrium among cable forces. Fig. 2 illustrates the force correlation of the segments. $\mathbf{G}_k$, $\mathbf{N}_k$, and $\mathbf{F}_k$ denote gravitational force, octahedral support force, and cable tension of k^{th} segment, respectively. The homogeneous transformation matrix from the j^{th} to the k^{th} segment is denoted as T_k^j. The reaction force on the octahedron of the $k+1^{st}$ segment at the k^{th} segment $\mathbf{N}_{k,k+1}$ is expressed as:

$$\mathbf{N}_{k,k+1} = -{T_{k+1}^{k}}^{-1}\mathbf{N}_{k+1} \tag{2}$$

Introducing CDHRR parameters and applying the Newton-Euler approach, the force balance equation is obtained:

$$\mathbf{P}\begin{bmatrix}\mathbf{F}_k\\ \mathbf{N}_k\end{bmatrix} = \begin{bmatrix}-\mathbf{G}_k - \mathbf{N}_{k,k+1}\\ -\mathbf{M}_G^k - \mathbf{M}_N^{k+1}\end{bmatrix} \tag{3}$$

where $\mathbf{P}$ is parameter matrix, incorporating the length of octahedron l_{oct} and the radius of segment r. $\mathbf{M}$ is the torque of the force.

The solution of the 24-DoF CDHRR results in twelve free force variables, with quadratic programming employed to minimize cable tension. In other words, the following optimization problem is addressed in determining the force $\mathbf{F}_k$ in the k^{th} section.

$$\min \frac{1}{2}\begin{bmatrix}\mathbf{F}_k\\ \mathbf{N}_k\end{bmatrix}^{\mathrm{T}}\mathbf{H}\begin{bmatrix}\mathbf{F}_k\\ \mathbf{N}_k\end{bmatrix} \tag{4}$$

where $\mathbf{H}$ is the penalty parameter matrix to avoid force overruns. Force constraints are set as:

$$\begin{bmatrix}200-15k\\ -\infty\end{bmatrix} \le \begin{bmatrix}\mathbf{F}_k\\ \mathbf{N}_k\end{bmatrix} \le \begin{bmatrix}200\\ \infty\end{bmatrix} \tag{5}$$

IV. Hybrid Tension and Configuration Closed-Loop Controller

A. Single-segment Controller

We propose a hybrid closed-loop control method to prevent cable failure. It integrates force control with position control, as is depicted in Fig. 4. Calculations are based on the current angle to determine the discrepancy between the target and the subsequent angle. The position closed-loop control is shown as follows:

$$\mathbf{D}_\theta = \mathbf{T}_\theta - \mathbf{A}_\theta \tag{6}$$

$$\mathbf{D}_{P\theta} = P_\theta \mathbf{D}_\theta \tag{7}$$

where $\mathbf{T}_\theta$ is the target angle. $\mathbf{A}_\theta$ is the current value of the horizontal and vertical angles measured by the robot's joint angle sensor. $\mathbf{D}_\theta$ is the difference between the robot's target angle and the current angle. $\mathbf{D}_{P\theta}$ is the angle of the robot's

This article has been accepted for publication in IEEE Robotics and Automation Letters. This is the author's version which has not been fully edited and content may change prior to final publication. Citation information: DOI 10.1109/LRA.2025.3559829

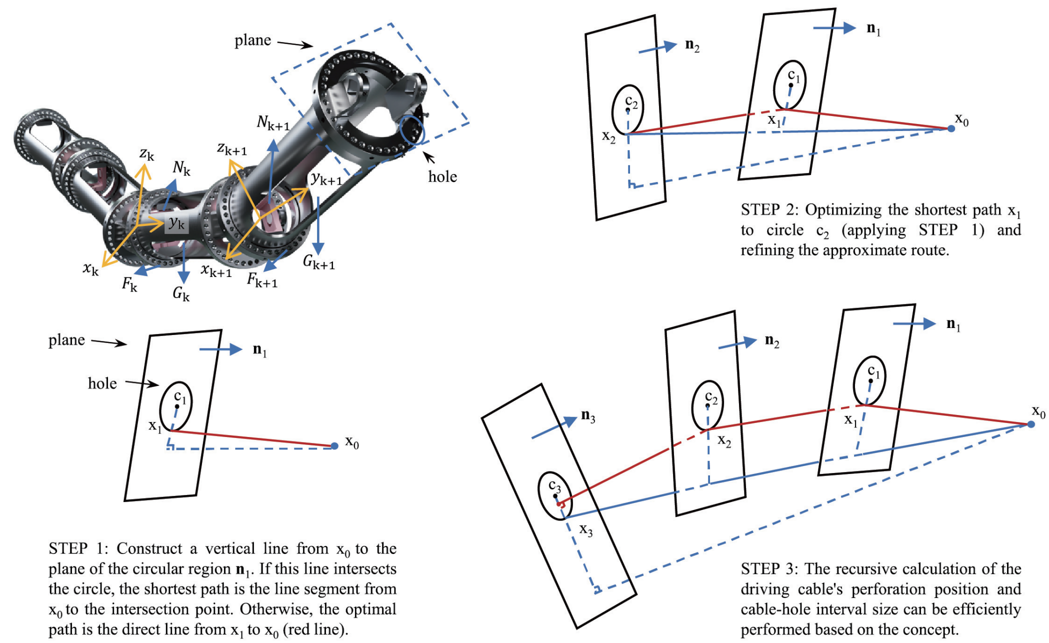

Fig. 2. Schematic diagram of the Cable-hole length estimation algorithm. x, c, and $\mathbf{n}$ denote intersection, center of circle, and normal vector, respectively. The cable guide disk, outlined in the upper dashed box, is modeled as a black plane with apertures. Auxiliary lines are depicted in blue, and operational cable states are denoted by red lines. (upper left) Force relationships between adjacent segments. The yellow arrows denote the coordinate system, and the blue arrows denote the forces on the segments. (lower left) Cable length estimation for CDHRR based on cable-hole interval calculation.

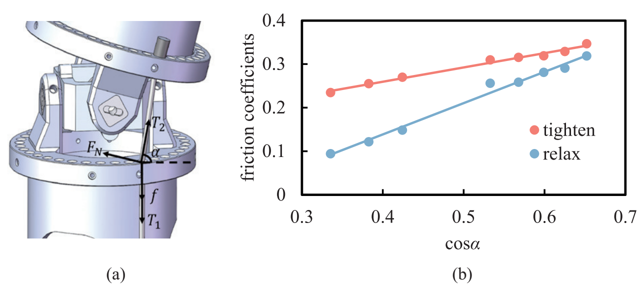

Fig. 3. (a) Force analysis diagram at the cable-hole. T_1 and T_2 are the tensions on the first and second segment, respectively. F_N is the support force at the contact location of the cable-hole. f is the cable-hole friction. α is the angle between neighboring segments. (b) Linear fitting of friction coefficients at different tilt angles. The coefficients correlate with the tilt angle and the process of stretching-relaxing.

motion in the next frame. P_θ is the scaling factor of the joint angle closed-loop control.

If the cable relaxation length in one frame is excessive, the joint angle will remain unaffected by subsequent cable tension adjustments. Therefore, the force closed-loop controller is designed:

$$\Delta F_j = F_{tj} - F_{rj} \tag{8}$$

$$\Delta q_{Fj} = P_F \Delta F_j \tag{9}$$

$$\Delta q_{aFj} = \Delta q_{aj} - \Delta q_{Fj} \tag{10}$$

where F_{tj} is the ideal tension of the j^{th} cable, F_{rj} is the actual tension measured on the j^{th} cable force sensor, Δq_{Fj} is the size of the corrected driving amount estimated according to ΔF_j, ΔF_j is the difference between F_{tj} and F_{rj}, P_F is the proportionality coefficient of the force closed-loop control, Δq_{aFj} is the theoretical driving amount of the j^{th} cable after the correction of the force closed-loop control, and Δq_{aj} is the theoretical driving amount of the j^{th} cable before the correction of the force closed-loop control.

The roles of the driving cables are differentiated according to Δq_{aFj}. They are categorized into 'stretching' and 'relaxing' cables, as shown in Fig. 4(a). F_{max} and F_{min} are the maximum and the minimum tensions, respectively. If the tension exceeds F_{max} or is below F_{min}, set Δq_{aFj} to 0.

B. Multi-segment controller

Algorithm 1 Multi-Segment Hybrid Controller

Input: Current target angles $\mathbf{T}_\theta$ and current angles $\mathbf{A}_\theta$.
Output: Cable driving amount Δq_{aFj}.

```
while TRUE do
    Δq_aj, Δq_cj, Δq_tj ← CABLE LENGTH CALCULATION ALGORITHM.
    Δq_Fj ← QUASI-STATIC MODEL(T_θ, A_θ)
    FORCE AND POSITION CLOSED-LOOP CONTROL.
    T_jx, T_jn, A_θ ← Updating force and angle data.
    Δq_aFj ← Δq_aj, Δq_cj, Δq_tj, and Δq_Fj.
    if Δq_aFj > 0 then
        Mark cables as stretching.
    else
        Mark cables as relaxing.
    end if
    if T_j is out of range then
        Δq_aFj ← 0.
    end if
end while
return Δq_aFj.
```

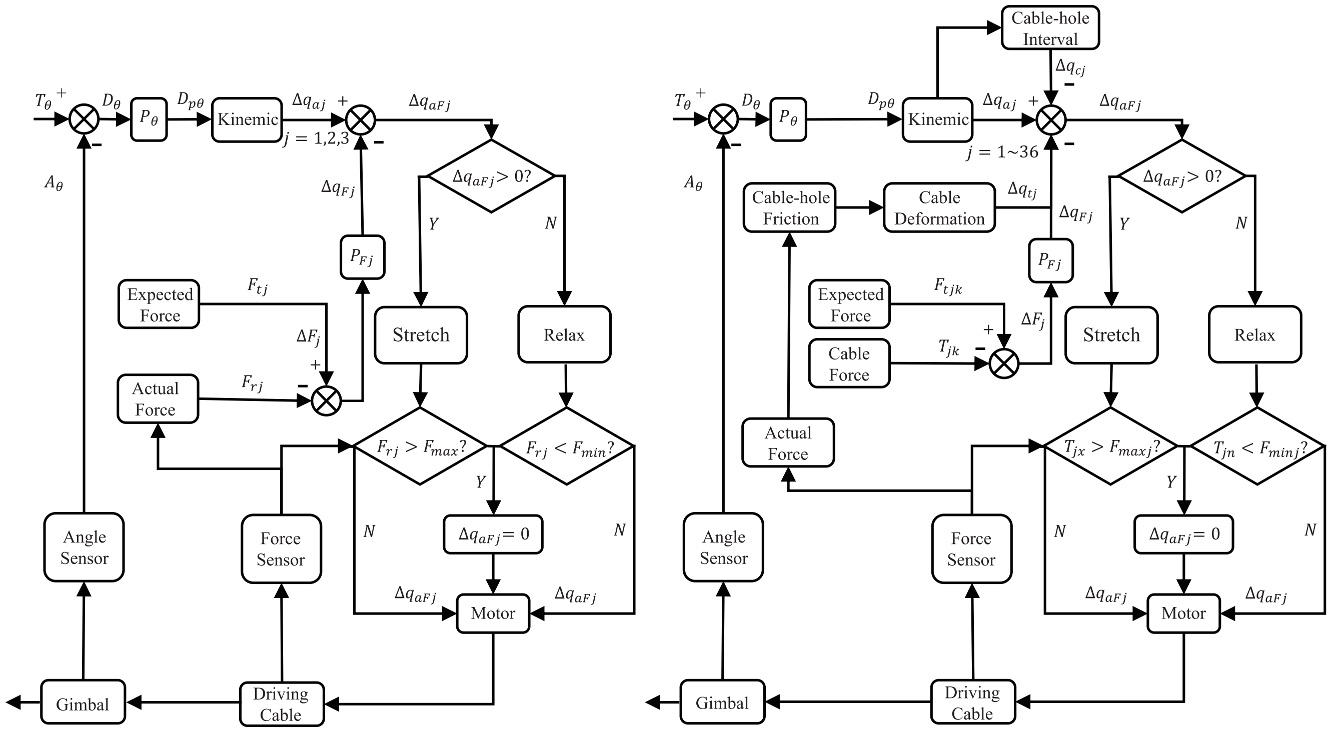

(a) (b)

Fig. 4. Design of (a) single-segment and (b) multi-segment hybrid configuration controllers. Relative to single-segment controllers, multi-segment controllers require the management of inter-segment coupling and antagonistic forces. Furthermore, the impact of error factors (i.e., the cable-hole interval, the cable deformation, and the cable-hole friction) is also considered.

To execute collaborative control across all segments, a multi-segment controller is engineered, which is introduced in Algorithm 1 to manage the coupling and antagonistic forces. Furthermore, error factors (i.e., cable-hole friction, cable-hole interval, and cable deformation) are integrated into the control strategy. The theoretical driving amount of the position closed-loop control is listed as:

$$\Delta q_{aFj} = \Delta q_{aj} - \Delta q_{Fj} - \Delta q_{cj} - \Delta q_{tj} \tag{11}$$

where Δq_{aFj}, Δq_{aj}, Δq_{Fj} have the same definitions as in the single-segment controller. Δq_{cj} is the cable-hole interval error, Δq_{tj} is the cable deformation error. They are solved by the model proposed in Section III.

For force closed-loop control, the force employed for calculation is estimated by sensor data. The force is ascertained through an analysis of cable-hole conditions. The formula for the force closed-loop correction is obtained as follows:

$$\Delta F_{jk} = F_{tjk} - T_{jk} \tag{12}$$

$$\overline{T_j} = \frac{\sum_{k=1}^{n^j_{sec}} T_{jk}}{n^j_{sec}} \tag{13}$$

$$P_{Fjk} = \frac{P_F \overline{T_j}}{T_{jk}} \tag{14}$$

$$\Delta q_{Fj} = \sum_{k=1}^{n^j_{sec}} P_{Fjk} \Delta F_{jk} \tag{15}$$

where F_{jk} is the discrepancy between the target and the actual force at the k^{th} segment of the j^{th} cable. The drive correction Δq_{Fj} is defined in the same way as in the single-segment controller, but it is necessary to sum up the drive corrections generated by all the cable segments. The definitions of F_{maxj} and F_{minj} are the same as in the single-segment controller. Other parameters are explained in Table II.

TABLE II
EXPLANATION OF PARAMETERS IN EQUATIONS 12–15

Symbol	Meaning
F_j	the force on j^{th} segment
n^j	the number of segments on the j^{th} cable
$\overline{T_j}$	the average value of all T_{jk}
P_{Fjk}	the k^{th} element of P_{Fj}
P_F	the value of the P control
T_{jx}	the maximum value of all T_{jk}
T_{jn}	the minimum value of all T_{jk}

As long as the tension of the corresponding driving cable is not between F_{minj} and F_{maxj}, the controller should issue a zero-drive amount. It is prioritized to ensure the safety of the controller. To ensure the consistency of actuation correction, P_{Fjk} will vary in tandem with changes in T_{jk}. That is, the controller focuses on the deviation between the desired and actual forces as a proportion of the desired force, irrespective of the magnitude of the desired force itself. The driving correction q_{Fj} is defined similarly to that in single-segment control. However, it encompasses the aggregate of driving corrections from all cable parts. The theoretical actuation extent derived from the position of closed-loop output mirrors that of the single one. Conversely, the actual force implemented for closed-loop computations is no longer equivalent to the sensor's force measurement. The tension correction also parallels the single-segment approach. However, it necessitates evaluating all segment forces to ascertain if the prevailing tension aligns with the target range.

C. Stepwise Force Arrangement

CDHRRs are susceptible to instability in control tasks. As the deformation of the actuation cable increases, the position closed-loop controller augments the tension to counteract the deformation. This exacerbates the unstable condition, leading to cable failure once the tension limit is surpassed. Therefore, the stepwise force arrangement is introduced to calculate desired tension. F_{tjk} in the force closed-loop control is set as:

$$F_{tjk} = F_t - F_{step}\lfloor\frac{j}{3}\rfloor \tag{16}$$

where F_t is desired force. F_{step} is stepwise force. Both F_t and F_{step} are ascertained via a combination of theoretical derivation and empirical validation. The desired tension ensures the cable is neither insufficient for control nor excessive to cause instability.

TABLE III
IDEAL FORCE FOR EACH SEGMENT

No.	$F_{k,1}$	$F_{k,2}$	$F_{k,3}$	No.	$F_{k,1}$	$F_{k,2}$	$F_{k,3}$
1	203.11	200.00	200.00	7	103.11	100.00	103.11
2	153.37	150.00	150.62	8	102.75	100.00	103.37
3	153.53	150.00	151.23	9	102.31	100.00	103.53
4	153.59	150.00	151.79	10	101.79	100.00	103.59
5	103.53	100.00	102.31	11	61.23	60.00	63.53
6	103.37	100.00	102.75	12	40.78	40.00	44.22

Table III is calculated by the model derived in Section III. $F_{k,i}$ is the tension on i^{th} cable of segment No. k. It shows the ideal force requirements for each segment. The theoretical results marginally underestimate the actual operational scenarios, which is attributed to cable-hole friction.

V. Experimental Validation

A. Structural Optimization

The optimization of the robot structure is shown in Fig. 1(c). Compared to the SJTU-Snake II, the thickness of the cable guide disk is reduced from 8 mm to 6 mm, and the weight is reduced from 31.18 g to 27.01 g. The weight of the segment is reduced from 83.12 g to 49.13 g. Table IV shows the experiments on friction reduction during stretching-relaxing process. The plastic coating of the steel wire cable deteriorates rapidly, and slight wear is observed on the bushing. Self-lubricating bushings can be used for larger diameters of the CDHRR design. The driving cable can choose steel wire or PBO according to specific scenario.

TABLE IV
FRICTION COEFFICIENT OF DIFFERENT ROPES

Cable type	Stretching coefficient	Relaxing coefficient
Steel with coat	0.34	0.25
Steel with bush	0.21	0.11
Polyethylene	0.20	0.15
Aramid	0.23	0.18
PBO	0.22	0.12

B. Validation of Hybrid Control

To verify the single-segment hybrid controller, the rear segment is controlled to move at specified angles. The horizontal and vertical angles are modulated from an initial state of 0° to 10.00° and subsequently from 10.00° back to 0°. The angular variation as a function of time is depicted in Fig. 5. The controller exhibits swift responsiveness and precise control, fulfilling the criteria for CDHRRs.

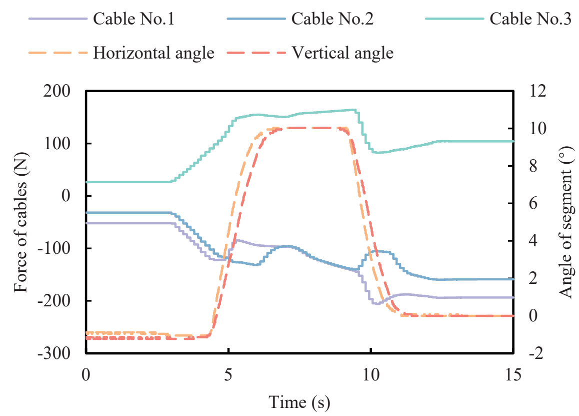

Fig. 5. Angular tracking performance and cable force distributions. The initial angular, starting from 0°, is calibrated by sequentially adjusting the three actuation cables in an open-loop configuration. Consequently, a substantial zeroing discrepancy emerged, with the deviation approximating 1.00°. After 2.9 s, the controller adjusted the horizontal and vertical angles to 10.03°, reducing the error by 97.0%. Following the second command, the controller adjusted the horizontal and vertical angles to 0.09° and 0° within 2.7 s, with an average error of 0.04°, thereby reducing the error by 95.6%.

As depicted in Fig. 5, the cable tensions fall within the force range, preventing both excessive slackness and potential breakage due to over-tightening. The cables' tension do not uniformly approach 200.0 N due to the intentional undersized P_F. It preserves the precision of the position loop control, and mitigates the impact of overwhelmed force control.

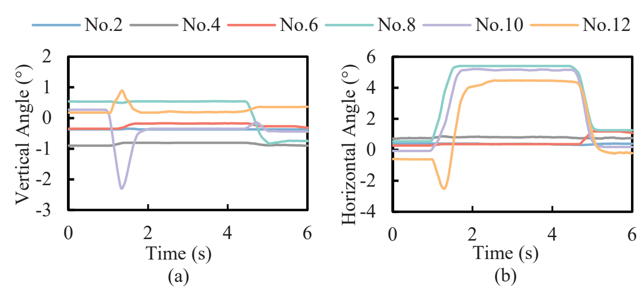

Fig. 6. Angular tracking performance. The command is to maintain the vertical angle while alternating the horizontal angle of the rear eight segments. (a) The vertical angles are maintained near the initial angle of 0° during the movement. (b) After 0.9 s, the controller adjusted the horizontal angles to around 5.00°, with an average error of 0.63°. After the second command, the controller adjusted all angles to around 0° within 1.0 s, with an average tracking error of 0.66°.

The angle variation curves of cables under multi-segment hybrid control are described in Fig. 6. All the horizontal angles of the rear eight segments (No. 5 to No. 12) can be actuated from an initial state of 0° to a final angle of 5.00°, while the first four segments (No. 1 to No. 4) are unaffected. Subsequently, the angles of all segments are reset to 0°. Relative to the single-segment controller, the average angular error may increase due to inter-segment interactions, which are still within the operational specifications for the SJTU-Snake III.

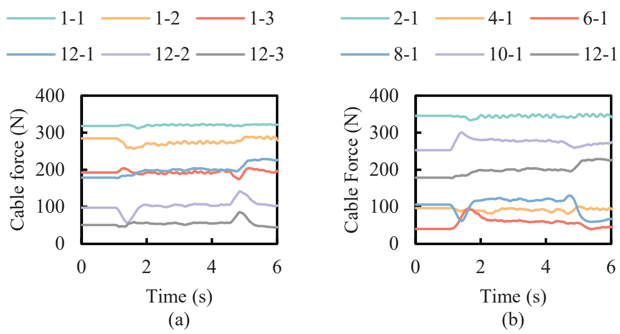

Fig. 7. Cable force distributions. The command is to maintain the vertical angle while alternating the horizontal angle of the rear eight segments. The '2-1' in the figure denotes the force sensor reading for the first actuation cable of the segment No. 2, and so on. F_{max} and F_{min} are set to 370.00 N and 60.00 N, respectively. F_t and F_{step} configured at 200.00 N and 10.00 N, respectively. (a) The tension on the driving cables was regulated between F_{max} and F_{min}. It fluctuated within a small range, and large fluctuations were flattened within 0.3 s. (b) The cable tension decremented sequentially from the 1^{st} to the 12^{th} segment, following the stepwise force configuration.

The tension variation of the cable is delineated in Fig. 7. Relative to the single-segment controller, the fluctuation scope of cable tension is further constricted. The P_F is increased to avoid the failure of the driving cable, and the step force is set to mitigate instability phenomena. The tension across all thirty-six cables is regulated between F_{max} and F_{min}, exhibiting minor fluctuations. Additionally, the controller is capable of rectifying significant fluctuations within 0.3 s. From segment No. 1 to No. 12, the tension gradually decreased, aligning with the stepwise force control objective. The undersized P_F results in a discrepancy between the cable tension and the target force. This phenomenon arises as the position closed-loop accuracy takes precedence, diminishing the impact of the force closed-loop control on the actuator's driving length. The experiment confirms the hybrid control system's ability to integrate force and position feedback, enhancing system responsiveness and accuracy.

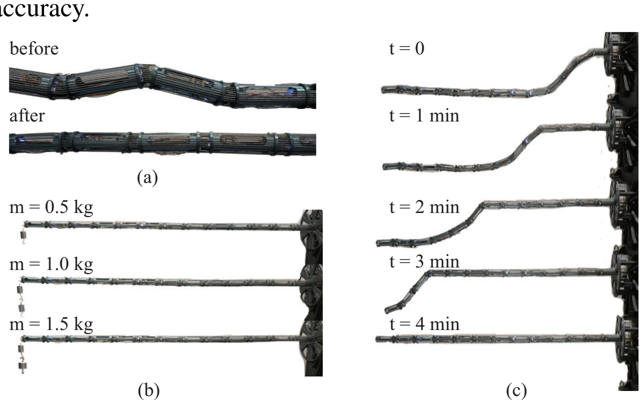

Fig. 8. (a) Automatic zeroing without and with hybrid configuration control method. The unstable state arises in the absence of the proposed controller, leading to control system instability or even cable failure. The implementation of stepwise force enhances the stability of the system. (b) Demonstration of automatic zeroing with loads of 0.5 kg, 1.0 kg, and 1.5 kg. (c) Demonstration of automatic zeroing facilitated by hybrid configuration closed-loop control. The zeroing process is completed in 4 mins.

As depicted in Fig. 8(a), instability is mitigated with the control strategy employing stepwise force. Reducing the step force incrementally precludes instabilities across segments. The hybrid control algorithm rectifies the W-shaped configuration resulting from antagonistic forces.

C. Automatic Zeroing and Tip-Loading

Cable tension facilitates automatic zeroing initialization, but relax state impedes it due to lack of initial tension. Conventional manual procedures are inefficient, impeding the operational effectiveness of CDHRR, particularly in scenarios that preclude intervention, such as nuclear inspections. A hybrid control-based fully automatic zeroing controller is designed, verifying tension compliance and modulating it to zero via single-segment controllers sequentially across all twelve segments. The safety factor is 1.5, initial segment force is 200 N, and the statics model-derived force serves as the desired actuation force for closed-loop control.

TABLE V
ANGLES OF SEGMENTS AFTER ZEROING

No.	Vertical	Horizontal	No.	Vertical	Horizontal
1	0.18°	0.17°	7	0.00°	0.00°
2	−0.27°	−0.64°	8	0.18°	−0.35°
3	−0.09°	0.18°	9	−0.35°	0.36°
4	0.81°	−0.81°	10	0.09°	0.00°
5	−0.80°	0.68°	11	−0.08°	−0.17°
6	0.18°	0.09°	12	0.18°	0.18°

Table V presents the angle of segments after zeroing. The mean angle error is 0.30°, with a peak deviation of 0.81°, satisfying the operational criteria for the CDHRR. In contrast, the previous generation SJTU-Snake II has a maximum error angle of 1.91°. The controller autonomously tensions the actuation cables for each segment sequentially before zeroing. It enhances operational efficiency and establishes a foundation for exploring spaces that are challenging for manual intervention. As is illustrated in Fig. 8(b), the average angular deviation remains below 1.00°, and the maximum angular deviation is within 1.50°, fulfilling the operational specifications. Fig. 8(c) reveals the zeroing time has been dramatically reduced to 4 minutes, while the previous robot takes as long as 1 hour to accomplish the same task.

VI. Conclusion

In this work, a novel hybrid tension and configuration closed-loop control method is introduced to tackle the challenges of imprecision and instability associated with CDHRRs. To actualize this approach, SJTU-Snake III is utilized for the physical construction and modeling of the system. Moreover, cable-specific error factors (cable-hole interval, cable-hole friction, and cable deformation) are incorporated to enhance model accuracy, achieving a mean angle error of less than 0.30°. Furthermore, algorithms for hybrid controller design, both single and multi-segmented, are designed based on the refined model. The experimental results demonstrate that the developed controller facilitates rapid automatic zeroing within 4 mins, and achieves mean errors ranging from 0.5% to 1.5% across diverse loads of 0.5 to 1.5 kg. Future work will focus on refining the model's precision by delving deeper into the study of friction and instability.

REFERENCES

[1] S. Ma, B. Liang, and T. Wang, "Dynamic analysis of a hyper-redundant space manipulator with a complex rope network," *Aerospace Science and Technology*, vol. 100, p. 105768, 2020.

[2] Z. Mu, T. Liu, W. Xu, Y. Lou, and B. Liang, "A hybrid obstacle-avoidance method of spatial hyper-redundant manipulators for servicing in confined space," *Robotica*, vol. 37, no. 6, pp. 998–1019, 2019.

[3] Z. Zhang, L. Zheng, J. Yu, Y. Li, and Z. Yu, "Three recurrent neural networks and three numerical methods for solving a repetitive motion planning scheme of redundant robot manipulators," *IEEE/ASME Transactions on Mechatronics*, vol. 22, no. 3, pp. 1423–1434, 2017.

[4] S. Coemert, A. Gao, J. P. Carey, M. F. Traeger, R. H. Taylor, T. C. Lueth, and M. Armand, "Development of a snake-like dexterous manipulator for skull base surgery," in *2016 38th Annual International Conference of the IEEE Engineering in Medicine and Biology Society*, 2016, pp. 5087–5090.

[5] D. Alatorre, B. Nasser, A. Rabani, A. Nagy-Sochacki, X. Dong, D. Axinte, and J. Kell, "Teleoperated, in situ repair of an aeroengine: Overcoming the internet latency hurdle," *IEEE Robotics & Automation Magazine*, vol. 26, no. 1, pp. 10–20, 2019.

[6] G. Qin, Y. Cheng, H. Pan, W. Zhao, S. Shi, A. Ji, and H. Wu, "Systematic design of snake arm maintainer in nuclear industry," *Fusion Engineering and Design*, vol. 176, p. 113049, 2022.

[7] M. Ivanescu and V. Stoian, "A controller for hyper-redundant cooperative robots," in *Proceedings. 1998 IEEE/RSJ International Conference on Intelligent Robots and Systems. Innovations in Theory, Practice and Applications*, vol. 1, 1998, pp. 167–172 vol.1.

[8] L. Tang, J. Wang, Y. Zheng, G. Gu, L. Zhu, and X. Zhu, "Design of a cable-driven hyper-redundant robot with experimental validation," *International Journal of Advanced Robotic Systems*, vol. 14, no. 5, p. 172988141773445, 2017.

[9] J. Tang, Y. Zhang, F. Huang, J. Li, Z. Chen, W. Song, S. Zhu, and J. Gu, "Design and kinematic control of the cable-driven hyper-redundant manipulator for potential underwater applications," *Applied Sciences*, vol. 9, no. 6, p. 1142, 2019.

[10] W. Xu, T. Liu, and Y. Li, "Kinematics, dynamics, and control of a cable-driven hyper-redundant manipulator," *IEEE/ASME Transactions on Mechatronics*, vol. 23, no. 4, pp. 1693–1704, 2018.

[11] F. Qi, B. Chen, S. Gao, and S. She, "Dynamic model and control for a cable-driven continuum manipulator used for minimally invasive surgery," *The international journal of medical robotics + computer assisted surgery: MRCAS*, vol. 17, no. 3, p. e2234, 2021.

[12] D. Jakes, Z. Ge, and L. Wu, "Model-less active compliance for continuum robots using recurrent neural networks," in *2019 IEEE/RSJ International Conference on Intelligent Robots and Systems*, 2019, pp. 2167–2173.

[13] M. Giorelli, F. Renda, G. Ferri, and C. Laschi, "A feed-forward neural network learning the inverse kinetics of a soft cable-driven manipulator moving in three-dimensional space," in *2013 IEEE/RSJ International Conference on Intelligent Robots and Systems*, 2013, pp. 5033–5039.

[14] J. Wang, C. Wu, and X.-J. Liu, "Performance evaluation of parallel manipulators: Motion/force transmissibility and its index," *Mechanism and Machine Theory*, vol. 45, no. 10, pp. 1462–1476, 2010.

[15] I. Vladu, D. Strîmbeanu, M. Ivănescu, N. Bîzdoacă, C. Vladu, and M. Florescu, "Control system for a hyper-redundant robot," *IFAC Proceedings Volumes*, vol. 45, no. 6, pp. 853–858, 2012.

[16] A. Dhyani, M. K. Panda, and B. Jha, "Design of an evolving Fuzzy-PID controller for optimal trajectory control of a 7-DOF redundant manipulator with prioritized sub-tasks," *Expert Systems with Applications*, vol. 162, p. 113021, 2020.

[17] A. Toedtheide, T. Lilge, and S. Haddadin, "Antagonistic impedance control for pneumatically actuated robot joints," *IEEE Robotics and Automation Letters*, vol. 1, no. 1, pp. 161–168, 2016.

[18] R. Cortez, M. A. Sandoval-Chileño, N. Lozada-Castillo, and A. Luviano-Juárez, "Snake robot with motion based on shape memory alloy spring-shaped actuators," *Biomimetics*, vol. 9, no. 3, p. 180, 2024.

[19] V. Potkonjak, B. Svetozarevic, K. Jovanovic, and O. Holland, "The puller-follower control of compliant and non-compliant antagonistic tendon drives in robotic systems," *International Journal of Advanced Robotic Systems*, vol. 8, no. 5, p. 69, 2011.

[20] Y. Zheng, Z. Li, J. Deng, J. Zou, G. Gu, and X. Zhu, "Improving the Motion Precision of a 24-DoF Hyper-Redundant Robot through Kinematic Calibration," in *2022 International Conference on Advanced Robotics and Mechatronics*, 2022, pp. 690–695.

[21] V. Stoian, N. Mircea, and M. O. Sorin, "Hybrid control for a hyper-redundant robot," in *15th International Conference on System Theory, Control and Computing*, 2011, pp. 1–5.

[22] V. Stoian and I. C. Vladu, "Hyper-redundant robot control system in compliant motions," in *Advances in Service and Industrial Robotics*, 2019, pp. 407–415.

[23] K. Zheng, "The improved force/position hybrid control system for multi joint humanoid multi fingered dexterous hand," *Journal of Mechanical Science and Technology*, vol. 38, no. 8, pp. 4343–4352, 2024.

[24] J. Peng, Y. Guo, D. Meng, and Y. Han, "Kinematics, statics modeling and workspace analysis of a cable-driven hybrid robot," *Multibody System Dynamics*, vol. 61, no. 2, pp. 163–193, 2024.

[25] Z. Li, J. Deng, Y. Zheng, C. Liu, and G. Gu, "Cable length estimation for a hyper-redundant robot based on cable hole clearance calculation," in *2023 IEEE 19th International Conference on Automation Science and Engineering*, 2023, pp. 1–7.